Neoplasma 2026; 73(2): 88–102

doi:10.4149/neo_2026_251111N475

(–)-Guaiol inhibits lung cancer via PPARG-dependent fatty acid oxidation

Zhen-Yu ZHAO[1,#], Bo ZHANG[1,#], Ying-Bin LUO[1], Xing-Yu WANG[2], Yu-Li WANG[1], Xi WANG[1], Jian-Hui TIAN[1], Jian-Chun WU[1,*], Yan LI[1,*]

[1]Oncology Department, Shanghai Municipal Hospital of Traditional Chinese Medicine, Shanghai University of Traditional Chinese Medicine, Shanghai, China; [2]Inner Mongolia Medical University, Hohhot, Inner Mongolia, China

**Correspondence: eq219@163.com; yanli6551@163.com; yan.xiaotian@shutcm.edu.cn*
#Contributed equally to this work.

Received November 11, 2025 / Accepted February 23, 2026

The objective of this study was to explore the effect of (–)-guaiol on lung cancer using experimental validation, mRNA sequencing, and network pharmacology. Potential targets of (–)-guaiol and lung cancer were identified through SwissTargetPrediction, TCMSP, PharmMapper, OMIM, GeneCards, and DisGeNET databases. Common targets were analyzed using PPI network, topological screening, and functional enrichment using STRING, Cytoscape, and Metascape. Molecular docking with core targets was performed, along with molecular dynamics. In vitro assays (cell counting kit-8 assay, colony formation, wound healing, Transwell, western blot) and in vivo studies (subcutaneous xenograft modeling in nude mice, immunohistochemistry, mRNA sequencing) were conducted to validate the anti-tumor effects and mechanisms of (–)-guaiol compared with the control group. Through multi-database prediction, 153 (–)-guaiol targets and 91 common lung cancer targets were identified. Protein-protein interaction (PPI) network analysis screened 21 core targets (including ESR1, EGFR, etc.). GO and KEGG enrichment analyses revealed that these targets are involved in the regulation of pathways such as fatty acid metabolism. Molecular docking and molecular dynamics results demonstrated that (–)-guaiol possessed a favorable binding affinity toward the target proteins SRC, PTGS2, GSK3B, PPARG, ESR1, and HSP90AA1. mRNA sequencing indicated that the gene expression levels of both PPARG and CD36 were downregulated in lung cancer tissues of mice treated with (–)-guaiol compared with the control group. Combining the results of molecular docking, molecular dynamics, and mRNA sequencing, we selected the PPARG-related signaling pathway for subsequent experiments. Both *in vivo* and *in vitro* experiments validated that (–)-guaiol inhibits lung cancer cell proliferation, invasion, and xenograft tumor growth in mice by downregulating the PPARG pathway. To conclude, our results demonstrated that (–)-guaiol suppresses lung cancer progression through downregulation of the fatty acid oxidation-related pathway mediated by PPARG.

Key words: (–)-guaiol; lung cancer; PPARG; network pharmacology; RNA-sequencing; in vitro; in vivo

Lung carcinoma continues to rank among the most prevalent malignancies globally, accounting for the greatest disease burden, including incidence and mortality rates [1]. Epidemiological studies show that the five-year survival probability among lung carcinoma cases remains below 20% [2], and advanced-stage patients exhibit low response rates to conventional chemotherapy and radiotherapy [3]. Despite advances in targeted therapies (e.g., EGFR inhibitors) and immune checkpoint blockade (e.g., anti-PD-1/PD-L1), drug resistance and the immunosuppressive tumor microenvironment persist as significant challenges [4]. Furthermore, the pathological mechanisms of lung cancer are complex, involving epithelial–mesenchymal transition (EMT), metabolic reprogramming (such as aberrant fatty acid oxidation), and the tumor-promoting functions of tumor-associated macrophages (M2-TAMs) [4, 5]. Therefore, exploring novel therapeutic targets and natural compounds to overcome the limitations of existing treatments is of great significance. In parallel, recent work has underscored terpenoid natural products as promising sources of multi-target agents capable of modulating oncogenic signaling and metabolic reprogramming in non-small cell lung cancer (NSCLC), supporting further exploration of sesquiterpene scaffolds such as (–)-guaiol as potential therapeutic candidates [6, 7].

PPARG, as a nuclear hormone receptor, a peroxisome proliferator-activated receptor (PPAR) family member, modulates both glucose and lipid metabolism, energy

homeostasis, and inflammatory responses. Increased PPARG expression is associated with poorer survival in breast cancer mice [8]. PPARG promotes lymph node metastasis of cholangiocarcinoma by upregulating fatty acid uptake and oxidation through an oleic acid-PPARG-fatty acid binding protein 4 positive feedback loop [9]. In addition, Tang et al. showed that compared to stage II HCC tissues, high expression of PPARG in TAMs of stage III HCC tissues significantly increased fatty acid oxidation [10]. It is noteworthy that PPARG is closely associated with the polarization of M2 macrophages in the neoplastic cellular milieu, which promotes lung cancer progression via secretion of IL-10 [6]. Therefore, targeting the PPARG-mediated fatty acid oxidation pathway may represent a novel therapeutic strategy for lung cancer.

(−)-Guaiol is a bicyclic sesquiterpene alcohol with a guaiane-type skeleton that is widely distributed in the essential oils of several traditional Chinese medicinal plants and coniferous species, and has been reported to exhibit antibacterial and antitumor activities [11]. Structurally, (−)-guaiol ($C_{15}H_{26}O$; molecular weight 222.37) contains a compact hydrophobic terpene framework bearing a single hydroxyl group, which confers low aqueous solubility but favorable membrane permeability typical of lipophilic terpenoids, properties that may influence its cellular uptake and distribution within tumor tissues. A simplified structural diagram of (−)-guaiol is provided in Supplementary Figure S1 (the picture is from the internet). Over the past few years, several studies have started to define the anticancer profile of (−)-guaiol in non-small cell lung cancer. Yang et al. showed that (−)-guaiol triggers immunogenic cell death in NSCLC, promotes dendritic cell maturation, enhances T-cell infiltration, and suppresses tumor growth *in vivo* [12]. Cao et al. further reported that (−)-guaiol inhibits EMT in lung cancer by suppressing M2 macrophage-mediated STAT3 signaling, thereby reducing the invasive and migratory capacity of NSCLC cells [13]. Earlier work also demonstrated that (−)-guaiol can regulate autophagic cell death in NSCLC through modulation of mTOR-dependent signaling [14]. Collectively, these studies indicate that (−)-guaiol exerts multi-faceted antitumor effects in NSCLC by impacting both tumor cell-intrinsic survival pathways and the tumor microenvironment. However, it remains unclear whether (−)-guaiol mediates anti-lung cancer activity by modulating fatty acid oxidation through PPARG.

Recent advances in network pharmacology have emphasized its interdisciplinary integration, and transcriptomics has provided novel insights for elucidating the multi-target mechanisms of natural products [7, 15]. Therefore, this study comprehensively applied network pharmacology, RNA sequencing, and both laboratory and animal studies to untangle the molecular mechanism through which (−)-guaiol inhibits lung cancer through the PPARG-mediated fatty acid β-oxidation route.

Materials and methods

Screening of (−)-guaiol and lung cancer target genes. Supplementary Figure S1 (from the internet) displays the molecular structure of (−)-guaiol. Supplementary Figure S2 illustrates the complete research workflow. Potential (−)-guaiol's targets were identified using SwissTargetPrediction analysis (https://www.swisstargetprediction.ch/), TCMSP (https://lsp.nwu.edu.cn/tcmsp.php/), and PharmMapper server (https://www.lilab-ecust.co.uk/pharmmapper/) databases. Concurrently, disease-associated targets related to lung cancer were retrieved from the OMIM (https://www.omim.org/), GeneCards (https://www.genecards.org/), and DisGeNet databases (https://www.disgenet.org/). The all-potential target proteins were standardized to official gene symbols using UniProt (https://www.uniprot.org/).

Acquisition of potential drug-disease common targets and construction of Venn diagrams. To identify the potential therapeutic targets of (−)-guaiol against lung cancer, the predicted target genes of (−)-guaiol and the lung cancer-related disease targets were compared. The intersection targets, representing the common genes between the drug and the pathological condition, were considered as potential key targets through which (−)-guaiol may demonstrate anti-lung cancer efficacy. The overlapping and unique targets were visualized via a Venn diagram created employing the jVenn online platform (https://jvenn.toulouse.inra.fr/app/example.html), which is part of the SRplot platform (https://www.bioinformatics.com.cn/static/others/jVenn/example.html).

PPI construction and critical target screening. The STRING database (https://www.string-db.org) was utilized to analyze shared targets and generate a human protein-protein interaction (PPI) network, with an interaction confidence score cutoff set above 0.4, with isolated nodes excluded, while other parameters retained their default settings. The protein interaction network was visualized with Cytoscape 3.10.0, followed by node screening based on topological characteristics. Critical network parameters (degree, betweenness, closeness) identified (−)-guaiol's primary lung cancer targets, facilitating development of a drug-target-disease model.

Establishing a "drug-target-pathway-disease" network. To systematically elucidate the pharmacological mechanism of (−)-guaiol against lung cancer, a comprehensive "drug-target-pathway-disease network was constructed. The network integrates the following key elements: the drug molecule (−)-guaiol, the disease (lung cancer), the common potential targets, and the key signaling pathways. This multi-layered network visualization and analysis were performed with Cytoscape (version 3.10.0). Network topology analysis was performed to identify hub nodes within the network. The degree centrality, a fundamental metric, was calculated for each node. The degree value represents the number of connections a node has, indicating its relative importance and influence in the network structure. Nodes with a higher degree value are considered more biologically significant.

The size of each node in the visualization was proportional to its degree value.

Analysis of GO functions and significant targets for KEGG pathway enrichment. To comprehensively elucidate the biological functions and related signaling pathways underlying the anti-lung cancer effects of (–)-guaiol, functional enrichment of the common targets was analyzed via Metascape (https://metascape.org/gp/index.html#/main/step1). The key targets were analyzed in Metascape using their official gene symbols, with *Homo sapiens* designated as the reference species. The research investigated Gene Ontology (GO) functional annotations – encompassing Biological Process (BP), Molecular Function (MF), and Cellular Component (CC) – alongside KEGG pathway analysis, and enrichment analysis was conducted. The statistical parameters were set as follows: a p-value cutoff <0.01, a minimum enrichment count threshold (odds ratio) of 1.5, and a minimal overlap requirement count (number of genes in a given term) of 3. All enriched terms were ranked in ascending order of p-value. The twenty most statistically significant enriched terms across gene ontology and KEGG analyses were selected for visualization. Bar graphs and bubble plots were created via the online data visualization tool SRplot (https://www.bioinformatics.com.cn/).

Molecular docking. Molecular docking analysis predicted candidate compound-target binding affinities. The binding affinity, indicated by negative binding energy, demonstrates the stabilization achieved when the ligand binds to its target protein; more negative values signify greater binding affinity of the active compound to the target protein. In this investigation, we conducted molecular docking simulations for (–)-guaiol targeting the seven highest-ranked core proteins ranked by degree (ESR1, EGFR, PPARG, PTGS2, HSP90AA1, SRC, and HMGCR). The structures of the small-molecule drug ligands were acquired from PubChem (https://pubchem.ncbi.nlm.nih.gov/), with target protein structures obtained from the Protein Data Bank (PDB) (https://www.rcsb.org/). Energy minimization of the ligands was conducted using Chem3D, while the acquired protein structures were standardized using AutoDockTools 1.5.6, including steps such as hydration and hydrogen addition. The docking experiments were performed using a blind molecular docking simulation approach. The molecular docking was performed to predict binding conformations and affinities. The outcomes were visualized and examined using PyMOL software.

Compound preparation and vehicle control. (–)-Guaiol (purity ≥99%) was dissolved in DMSO to prepare a 10 mM stock solution. Working concentrations were prepared by diluting the stock in complete culture medium. All experiments included a vehicle control group treated with 0.1% DMSO, matching the highest solvent concentration in treated groups.

Cell culture. The A549 cell line was sourced from the Chinese Academy of Sciences Cell Resource Center (Shanghai). A549 cells were maintained in high-glucose DMEM medium (KeyGEN BioTECH, #KGL1206-500) containing 10% fetal bovine serum (FBS; Gibco) with 1% penicillin-streptomycin, cultured at 37 °C in 5% CO_2. The experimental manipulations were generally performed when the cell growth was in the logarithmic phase.

CCK-8 experiments. Exponentially growing A549 cells were seeded at 3×10^4 cells/ml in 96-well plates, followed by medium aspiration after 24 h incubation, and then different concentrations of (–)-guaiol ($C_{15}H_{26}O$, molecular weight: 222.37, purity 99.0%, #HY-N3980, MedChemExpress, Monmouth Junction, USA) were added. Following 24 h treatment, the culture medium was removed, followed by the addition of 100 µl 10% CCK-8 solution (#BEB22001, BEB Laboratories, Nanjing, China). The compound was dissolved in DMSO, and the final DMSO concentration in all treatment groups, including the 0 µM control, did not exceed 0.1% (v/v). Control groups received an equivalent volume of DMSO as a vehicle. After a 4 h incubation, absorbance at 460 nm was measured at 37 °C. The antiproliferative effect was calculated using the formula: [1 – (treatment OD/control OD) × 100%.

Colony formation assay. Logarithmically growing A549 cells were plated in 6-well culture dishes at 1,000 cells/well, then treated with (–)-guaiol and maintained under standard conditions (37 °C, 5% CO_2) for 10–14 days. When macroscopic cell colonies were clearly visible to the naked eye, the medium was gently aspirated, followed by two PBS washes of the 6-well plate. Cell colonies were fixed using 4% paraformaldehyde for 30 minutes under ambient conditions (25 °C). After fixation, the colonies were incubated using 0.1% (w/v) crystal violet solution for 20 min under ambient conditions. Following PBS washing and air-drying, the stained colonies were photographed with a digital camera. The number of colonies (defined as clusters containing >50 cells) was counted using ImageJ software.

Wound healing experiments. Log-phase A549 cells were plated at 5×10^5 cells/well in 6-well plates. Before plating, three horizontal lines were drawn on the outer bottom of each well using a black marker to serve as reference points for image acquisition. After the cells reached approximately 80% confluence and were fully adhered, a uniform scratch was created using a sterile 200 µl micropipette tip, and the cell monolayer was treated. Subsequently, the detached cells underwent two PBS washes with gentle agitation before replenishment with (–)-guaiol-containing fresh medium in each well. The culture plates were then cultured at 37 °C with 5% CO_2. Photographs of the scratch wounds were obtained at the same predefined locations immediately after scratching (0 h) and after 24 h of incubation.

Transwell assay. Cell invasion potential was assessed using a Transwell migration assay. Following matrix polymerization, the lower chamber received 800 µl of DMEM containing 10% FBS (Corning #3422, USA) as a chemoattractant, while 200 µl cell suspension (5×10^4 cells/ml in serum-free DMEM) was carefully placed in the upper chamber and cultured for

24 h at 37 °C in 5% CO_2. Subsequently, the inserts were then extracted, the upper membrane's residual non-adherent cells were thoroughly cleared using cotton swabs, while migrated cells adhering to the lower membrane were fixed with 4% paraformaldehyde for 10 min, PBS-washed twice, and allowed to air-dry prior to 10 min staining with 0.1% crystal violet. Following drying at ambient temperature, photographs of the invaded cells were taken using an inverted microscope (Leica, MZ-10F, Germany) for subsequent quantification.

Western blot. After treatment with (−)-guaiol, cell lysates were generated with ice-cold RIPA buffer supplemented with phosphatase and protease inhibitors (1:1:50). Protein quantification was performed with the BCA Protein Quantification Kit (#PA115, TIANGEN, Beijing, China). Protein samples (50 μg/lane) were electrophoresed by SDS-PAGE and electroblotted onto PVDF membranes (#356234, Corning, USA) using following wet transfer, membranes were blocked with 5% skim milk and subsequently probed with primary antibodies overnight at 4 °C incubation, specifically: PPARG (1:1000, #YM1082, ImmunoWay, USA), CPT1A (1:1000, #22170-1-AP, Proteintech), CPT1B (1:1000, #15184-1-AP, Proteintech), CD36 (1:1000, #28109, Proteintech), and β-actin (1:3000). Subsequently, membranes were incubated with HRP-conjugated secondary antibody (1:10,000, #66009, Proteintech, Wuhan, China). Subsequently, the membranes were treated with HRP-linked secondary antibody (1:10,000, #SA00001, Proteintech) at ambient temperature for 1 h, followed by ECL visualization and ImageJ quantification of protein bands.

Animal modeling. All procedures involving animals complied with NIH animal care standards and were approved by the Ethics Committee for Experimental Animal Medicine of Shanghai Hospital of Traditional Chinese Medicine (Approval No. 2023047). Optimally proliferating A549 cells were selected and implanted subcutaneously (3×10^4 cells/mouse) in the right scapular area using 6-week-old Balb/c nude mice (Shanghai Jima Pharmaceutical Technology Co., Ltd., China). Drug treatment commenced 72 h post-inoculation: the control cohort was administered intraperitoneal injections of physiological saline solution (100 μl) every two days. In contrast, the experimental cohort was subjected to intraperitoneal injections of 8 mg/kg (−)-guaiol (100 μl) every two days. The operational procedure is illustrated in Supplementary Figure S3 (figure created via https://BioRender.com). Tumor progression in xenograft-bearing mice was tracked daily, recording growth parameters (size, mass, volume) and latency period from implantation to tumor establishment. Following a three-week period, the animals were euthanized via cervical dislocation, after which tumors were excised by blunt dissection, weighed, and volumetrically measured. Partial tumor tissues were collected for mRNA sequencing and immunohistochemical experiments.

Immunohistochemistry. After three weeks, the animals were euthanized via cervical dislocation, followed by tumor excision through blunt dissection, weighing, and volume measurement. Three weeks post-treatment, animals were euthanized via cervical dislocation, followed by tumor excision through blunt dissection with subsequent weighing and volumetric measurement. After overnight incubation with primary antibody at 4 °C, the tissue sections were incubated with HRP-conjugated secondary antibodies for 30 min at ambient conditions. DAB was used for chromogenic detection, followed by hematoxylin counterstaining, differentiation, and bluing. Finally, the tissue sections were dehydrated, cleared, and mounted with neutral balsam before microscopic imaging for quantitative assessment of positively stained regions.

mRNA sequencing. mRNA sequencing (mRNA-seq) is a high-throughput gene expression profiling technique capable of untangling differences in gene expression profiles across various cells or tissues in both breadth and depth, as well as detecting splicing variants generated by RNA catalysis. In recent years, this technology has achieved significant advancements and has been widely adopted. Compared to conventional genetic testing methods, mRNA-seq offers multiple advantages. In this experiment, six samples from both the control and experimental groups were preserved on dry ice and subsequently sent to Ouyi Biotechnology Co., Ltd. (Shanghai, China). Following a three-week period, the animals were euthanized via cervical dislocation, after which tumors were excised by blunt dissection, weighed, and volumetrically measured. Following quality evaluation of raw sequencing data, the filtered reads were aligned to the reference genome. Differentially expressed genes (DEGs) were determined by applying cutoff criteria of $|\log2FC|>1$ and q-value <0.05.

Statistical analysis. GraphPad Prism 8.0.2 was used to evaluate all experimental data. Each experiment was carried out at least three times. The Shapiro-Wilk test was used to determine whether the experimental data satisfied a normal distribution. Data that met normal distribution were analyzed for differences between groups using one-way ANOVA. Data that did not meet the normal distribution were analyzed using the Kruskal-Wallis analysis. Significant differences were defined as $p<0.05$.

Results

(−)-Guaiol and the acquisition of potential targets in lung cancer. The SwissTargetPrediction database identified 40 potential (−)-guaiol's targets, the TCMSP database contained 13 targets of (−)-guaiol, and the PharmMapper database identified 110 targets of (−)-guaiol. After removing duplicates, a compilation of 153 potential targets for (−)-guaiol was assembled. Additionally, a total of 446 lung cancer-related targets were obtained from the OMIM database; the GeneCards database identified 25,001 potential targets associated with lung carcinoma; the DisGeNET database additionally identified 4,173 targets linked to lung cancer. Comparative analysis of both target sets revealed 91

common targets between (–)-guaiol and lung cancer, visualized through a Venn diagram (Figure 1A).

PPI network of the common targets between (–)-guaiol and lung cancer. The 91 common targets identified for (–)-guaiol and lung cancer were analyzed for protein-protein interactions using the STRING database (https://www.string-db.org) and visualized through Cytoscape 3.10.0. Finally, the interaction network between (–)-guaiol and lung cancer targets was constructed. Degree values determined the nodes' size and color. There were a total of 90 nodes (representing 90 screened potential shared targets) and 418 edges (highlighting interconnections among 90 prospective shared targets), as depicted in Figure 1B.

Screening and visualization of key targets. Based on the analysis of node topological properties, the included data comprised node degree, betweenness centrality (BC), and proximity centrality (PC). The screening criteria were set as follows: node degree ≥10, betweenness centrality ≥0.017, and closeness centrality ≥0.4. Twenty-one potential key targets were identified, indicating their likely role in mediating (–)-guaiol's anti-lung cancer effects. Supplementary Table S1 presents the gene names, node degrees, betweenness centrality, and closeness centrality of these key targets. Figure 1C illustrates the interaction network of core targets. The seven highest-ranked targets based on node degree were: ESR1 (degree = 33), EGFR (degree = 32), PPARG (degree = 31), PTGS2 (degree = 29), HSP90AA1 (degree = 29), SRC (degree = 25), and HMGCR (degree = 24).

GO and KEGG functional enrichment analysis. The 21 core target genes were analyzed using Metascape for GO term enrichment analysis. The GO functional analysis revealed 22 cellular components, 39 molecular functions, and 507 biological processes. The top 20 highest-degree nodes from each category were selected for analysis, and the findings were displayed as histograms (Figure 2A) and bubble plots (Figure 2B). The 20 most highly enriched biological processes were: response to hormone, Nuclear receptors meta pathway, modulation of protein localization establishment, Cancer pathways, Downregulation of intracellular signal transduction, Regulation of systemic processes, Modulation of protein trafficking, Regulation of the MAPK cascade, Cellular response to hormonal stimuli, modulation of inflammatory reactions and suppression of apoptosis-related signaling cascades, upregulation of proteins transport, CKAP4 signaling pathway map, regulation of miRNA transcription, regulation of ncRNA transcription, Relationship between inflammation COX 2 and EGFR, Aryl hydrocarbon receptor pathway, PID AR TF PATHWAY. The first 20 cells were composed of vesicle lumen, glutamatergic synapse, membrane microdomain, dendritic tree, membrane raft, dendrite, axon, ficolin-1-rich granule lumen, distal axon, apical part of cell, cytoplasmic vesicle lumen, cell body, receptor complex, ficolin-1-rich granule, neuronal cell body, secretory granule lumen, cell projection membrane, endocytic vesicle, nuclear speck, early endosome. The 20 most significantly enriched molecular functions encompassed RNA polymerase II-specific DNA-binding transcriptional regulation by protein kinases functionality, protein kinase association, kinase interaction, kinase catalytic activity, The enriched molecular functions

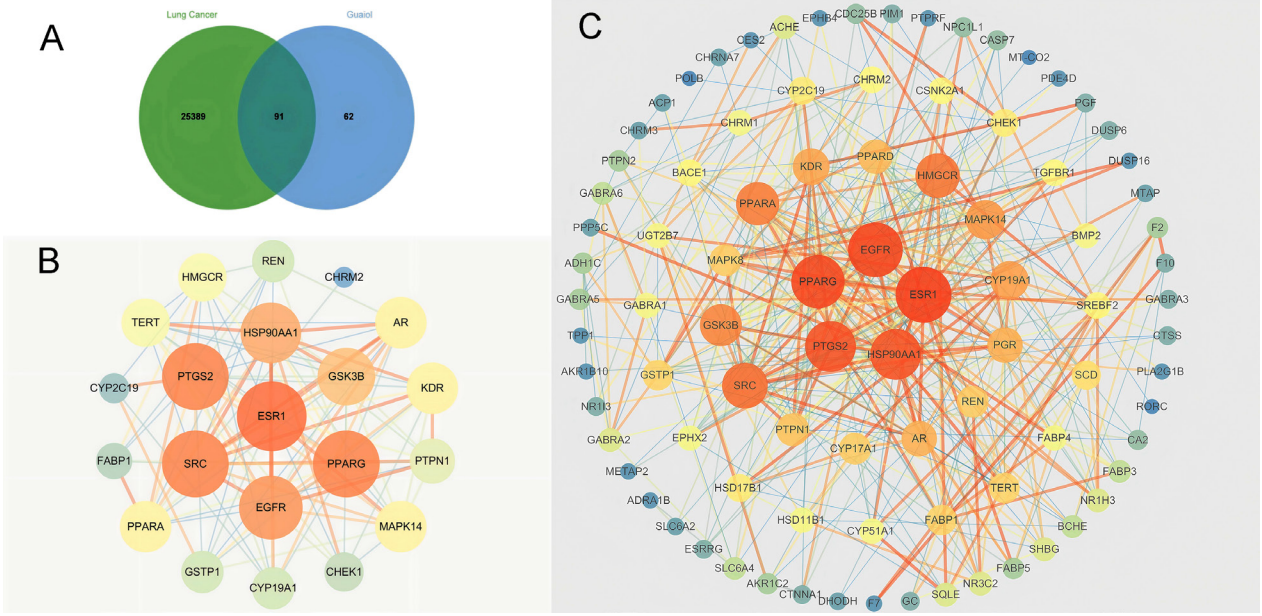

Figure 1. The common targets between (–)-guaiol and lung cancer screened by Network Pharmacology. A) Venn diagram showing the targets of the component-disease intersection. B) PPI network diagram of common potential targets between (–)-guaiol and lung cancer. C) Network diagram of (–)-guaiol interaction with key targets in lung cancer.

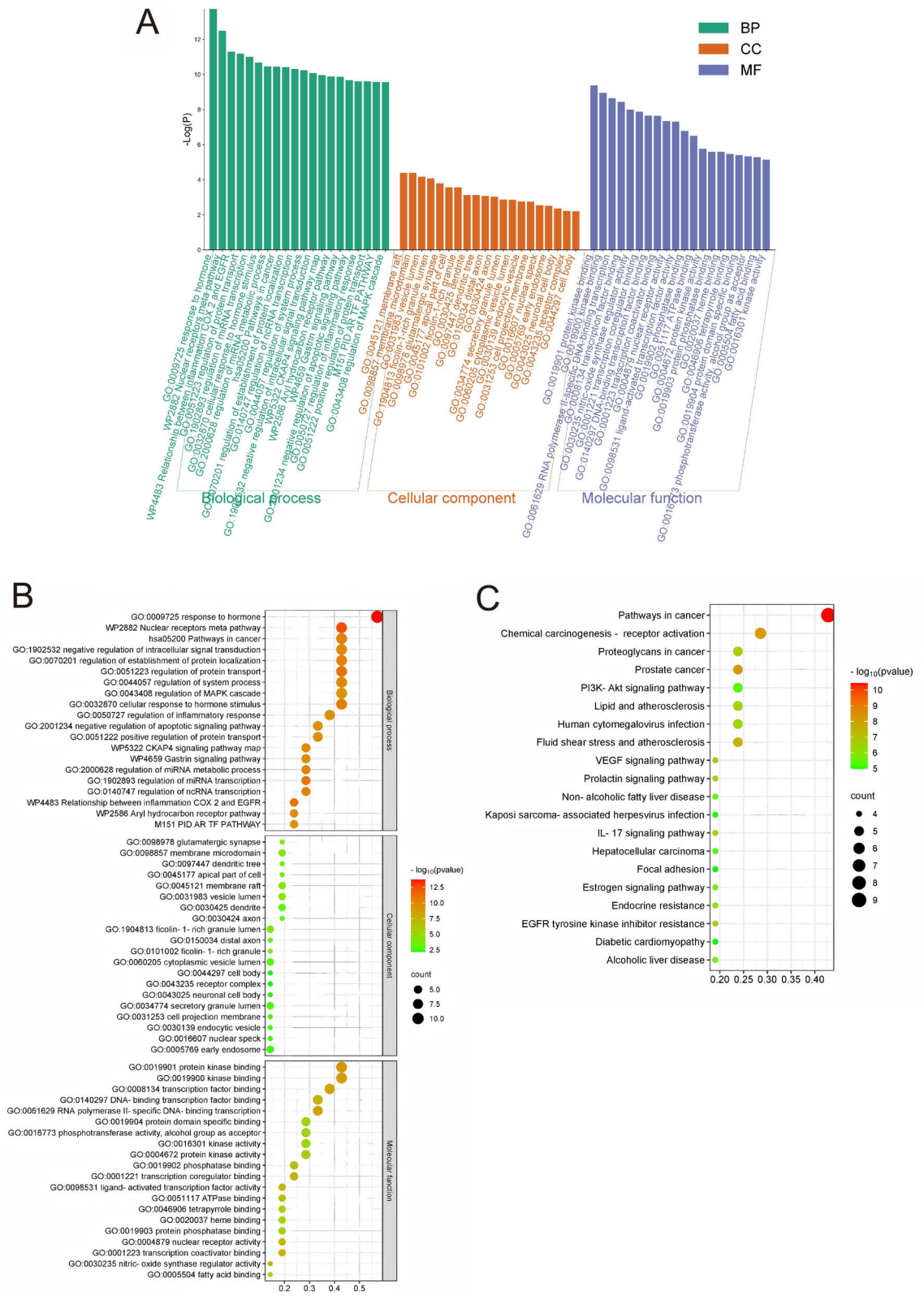

Figure 2. Go and KEGG enrichment analysis results. A) Histogram of the top 20 entries in the GO function enrichment analysis of genes. B) Bubble chart of the top 20 degree entries as a result of GO functional enrichment analysis. C) Bubble plot of the top 20 degree entries from KEGG enrichment analysis results.

comprised DNA-binding transcription factor interaction, phosphotransferase activity, transcription factor binding, alcohol group acceptor function, phosphatase association, protein domain-specific binding, transcription coregulator engagement, ligand-activated transcription factor function, ATPase association, tetrapyrrole binding, heme interaction, protein phosphatase binding, nuclear receptor function, transcription coactivator engagement, nitric-oxide synthase regulation, and fatty acid binding.

Twenty-one key targets were analyzed in Metascape for KEGG pathway enrichment, resulting in 45 significant signaling pathways. The top 20 KEGG pathways ranked by degree centrality were mapped and visualized as bubble plots (Figure 2C). The KEGG pathways and their associated targets are annotated in Supplementary Table S2. The 20 most enriched KEGG pathways were: Proteoglycans in cancer, Fluid shear stress in atherosclerosis, receptor-mediated chemical carcinogenesis, Oncogenic pathways, Lipid metabolism in atherosclerosis, Prostatic carcinoma, Cytomegalovirus infection in humans, Resistance to EGFR tyrosine kinase inhibitors, VEGF Signaling cascade, Prolactin-mediated signaling, Estrogen-mediated signaling, Non-alcoholic steatohepatitis, Kaposi sarcoma-associated herpesvirus infection, Hepatocellular carcinoma, Focal adhesion, Alcoholic liver disease, Endocrine resistance, Diabetic cardiomyopathy, The IL-17 and PI3K-Akt signaling cascades were visualized using Cytoscape software version 3.10.0 of (–)-guaiol with 21 key targets Top 20 signaling pathway and lung cancer, as shown in Figure 3.

Molecular docking and molecular dynamics. The binding of simulated drugs and disease targets was detected by molecular docking (Figures 4A–4G). Supplementary Table S3 shows the binding energy of (–)-guaiol to each key target. The results showed that (–)-guaiol bound well to all key targets, with the strongest binding to GSK3B, followed by SRC, ESR1, PTGS2, PTGS2, PPARG, HSP90AA1, and EGFR. The molecular docking showed that (–)-guaiol may elicit its anti-lung cancer effect by targeting these proteins.

Structural stability in protein-ligand systems was assessed using root-mean-square deviation (RMSD), with lower values indicating greater complex stability, as illustrated in Figure 5A, except for the EGFR-(–)-guaiol complex, the RMSD values of the complexes formed between SRC, PTGS2, GSK3B, PPARG, ESRI, and HSP90AA1 with (–)-guaiol reached equilibrium after 5 ns, eventually stabilizing at approximately 2.3 Å, 2.4 Å, 1.8 Å, 2.8 Å, 2.5 Å, and 4.7 Å, respectively, indicating high stability of these complexes. Evaluation of the gyration radius (Rg) (Figure 5B) revealed minor structural fluctuations during the simulation, with no significant expansion or contraction observed. The solvent-accessible surface area (SASA) (Figure 5C) further indicated no substantial change in surface area after binding, suggesting that ligand binding had a limited impact on protein conformation. Hydrogen bond analysis (Figure 5D) demonstrated that stable hydrogen bond interactions were maintained between (–)-guaiol and each target protein, with the number of bonds mostly ranging between one and two, and occasionally reaching three, indicating favorable binding specificity.

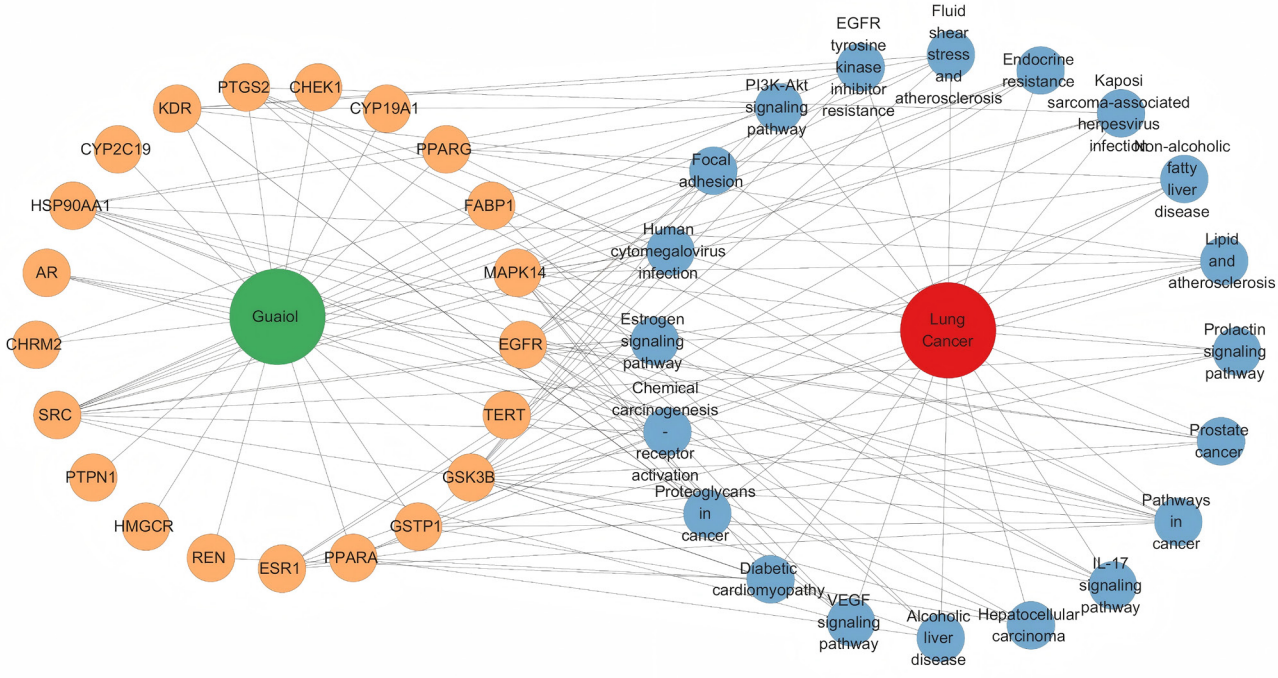

Figure 3. Network of relationships between (–)-guaiol, key targets, top 20 KEGG pathways, and lung cancer.

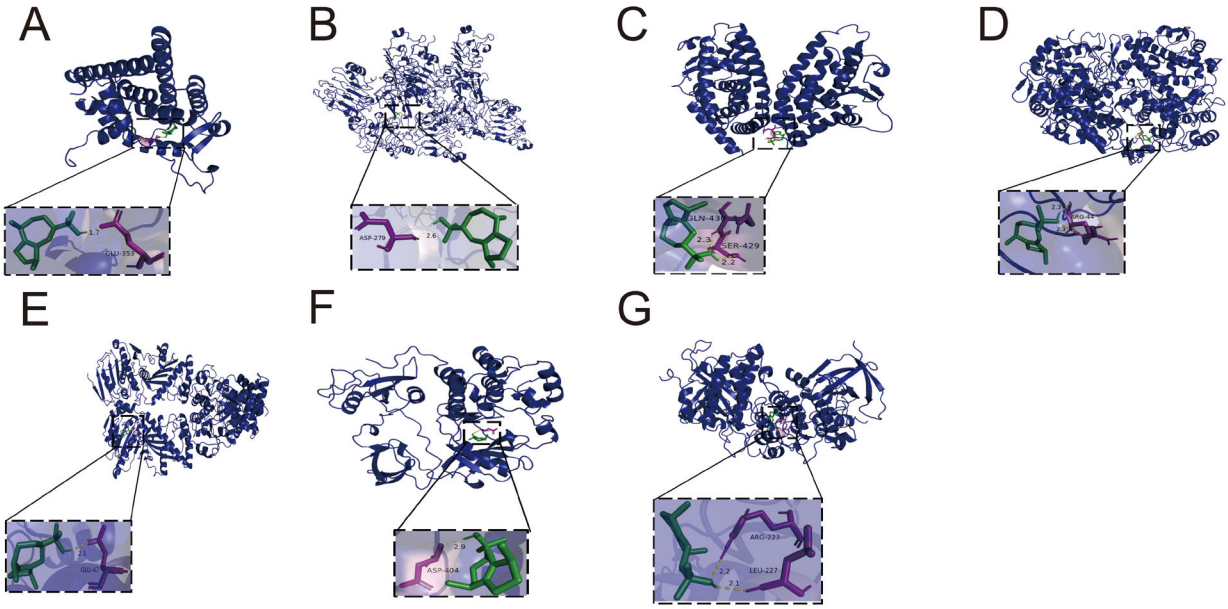

Figure 4. Molecular docking of (−)-guaiol with key targets. A) (−)-Guaiol-ESR1; B) (−)-Guaiol-EGFR; C) (−)-Guaiol-PPARG; D) (−)-Guaiol-PTGS2; E) (−)-Guaiol-HSP90AA1; F) (−)-Guaiol- src; G) (−)-Guaiol-GSK3B.

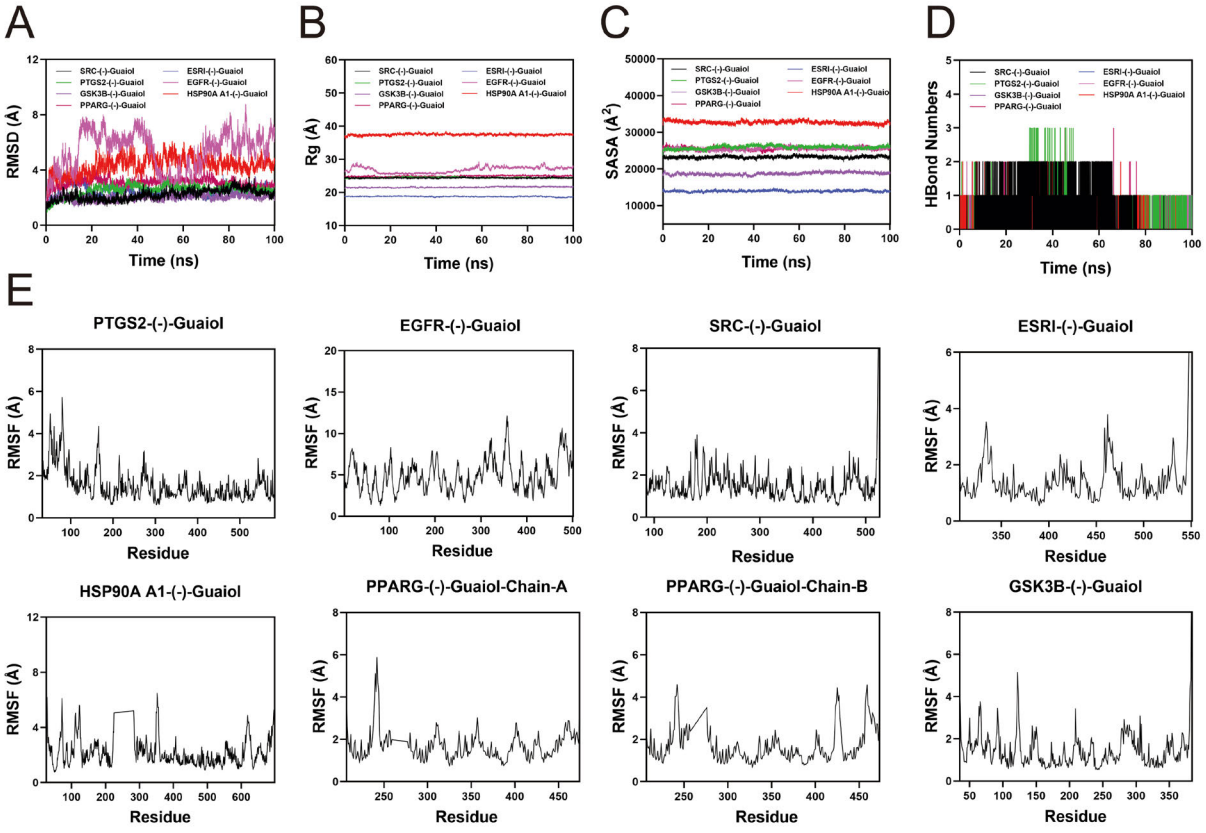

Figure 5. Molecular dynamics simulation of the protein-ligand complex. A) Root-mean-square deviation (RMSD) values of the protein-ligand complex over time; B) Radius of gyration (Rg) values of the protein-ligand complex over time; C) Solvent-accessible surface area (SASA) values of the protein-ligand complex over time; D) Number of hydrogen bonds (HBonds) in the protein-ligand complex over time; E) Root-mean-square fluctuation (RMSF) values of the protein–ligand complex.

Moreover, the root-mean-square fluctuation (RMSF) results (Figure 5E) showed that residue fluctuations in all complexes were mostly below 3 Å, suggesting low overall structural flexibility and high stability.

Subsequently, the binding free energy of ligand-protein complexes was computed using the MM/PBSA approach using its bound conformation (Figure 6A). This study further computed and analyzed the amino acid residues that contributed significantly to the binding of the small molecule within each complex system. The results indicated that in the SRC-(–)-guaiol complex, residues LEU407, ILE336, LEU325, LYS295, and MET314 exhibited high contribution values (Figure 6B). In the ESRI-(–)-guaiol complex, residues ILE424, MET421, LEU387, ALA350, MET388, LEU391, LEU428, and LEU525 showed high contribution values (Figure 6C). For the GSK3B-(–)-guaiol complex, residues PHE229, TYR288, and ILE228 were identified with high contribution values (Figure 6D). In the PTGS2-(–)-guaiol complex, residues LEU152, ARG469, GLN461, PRO153, and ASN39 demonstrated high contribution values (Figures 6E, 6F). In the PPARG-(–)-guaiol complex, residues SER429 and LEU431 were found to have high contribution values (Figure 6G). Lastly, in the HSP90AA1-(–)-guaiol complex, residues MET998, ASN51, PHE138, LEU107, ASN106, and ALA55 showed high contribution values (Figure 6H). These results indicate that these residues might be crucial for catalysis.

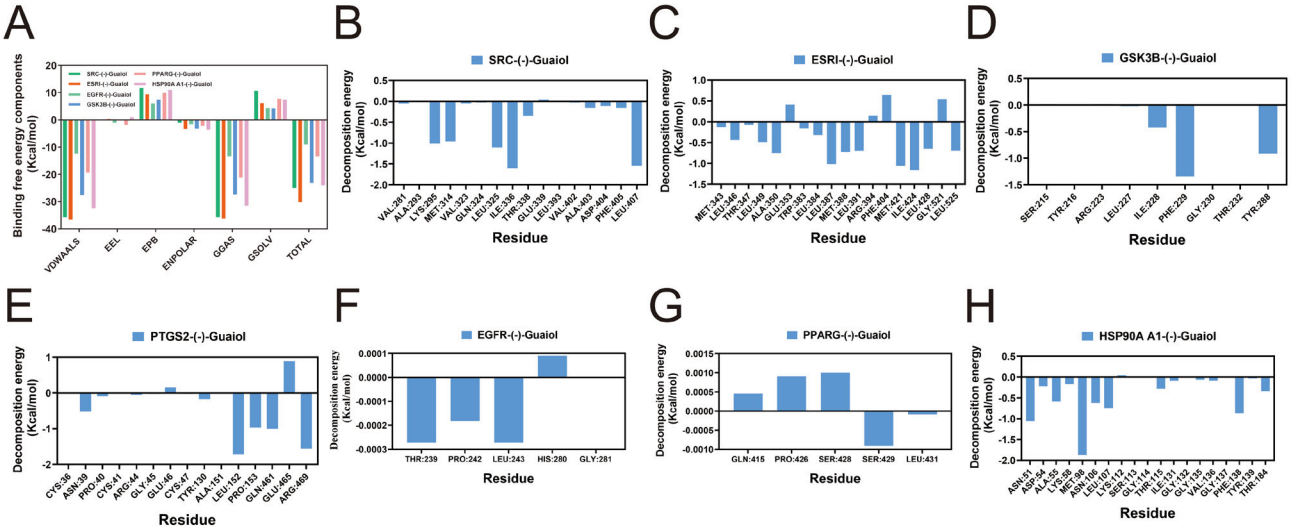

Figure 6. MMPBSA binding free energy calculation. A) binding free energy; B-H) the amino acid residues that contributed significantly to the binding of the small molecule within each complex system.

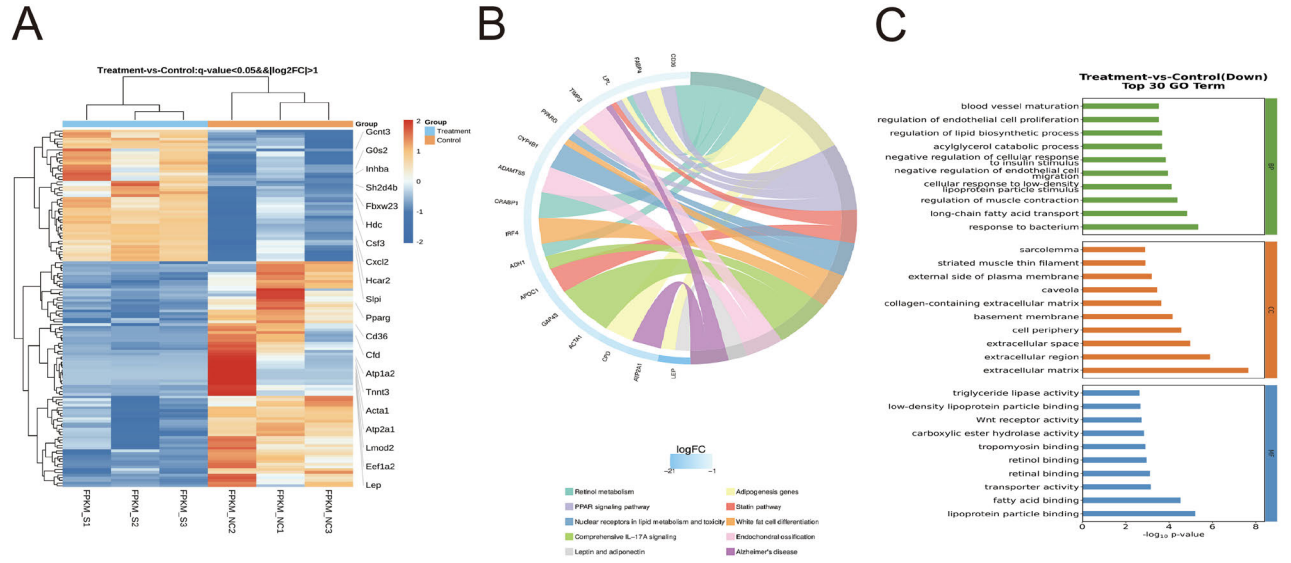

Figure 7. mRNA sequencing results. A) Differential gene expression level clustering analysis. B) WikiPathways enrichment analysis and chord plot. C) WikiPathways enrichment analysis.

In summary, the complex systems of SRC-(−)-guaiol, PTGS2-(−)-guaiol, GSK3B-(−)-guaiol, PPARG-(−)-guaiol, ESR1-(−)-guaiol, and HSP90AA1-(−)-guaiol all exhibited stable binding conformations, with robust hydrogen bond interactions observed in each complex. These results indicate that the small molecule (−)-guaiol possesses a favorable binding affinity toward the target proteins SRC, PTGS2, GSK3B, PPARG, ESR1, and HSP90AA1.

mRNA sequencing. Through mRNA sequencing analysis of lung cancer tissues from the control and experimental groups (n=3), a total of 24,443 genes expressed in at least one sample were identified. Gene expression analysis detected 22,609 transcripts in controls versus 22,692 in treated samples, with differential expression analysis identifying 49 upregulated and 84 downregulated genes relative to controls. Comparative analysis revealed downregulated expression of both PPARG and CD36 genes in (−)-guaiol-treated murine lung cancer tissues relative to controls (Figure 7A). The PPARG signaling pathway was pinpointed as a pivotal pathway mediating (−)-guaiol inhibition on lung cancer (Figure 7B). GO analysis further indicated that (−)-guaiol can inhibit triglyceride lipase activity (Figure 7C). Based on these findings, we speculate that (−)-guaiol may suppress lung cancer by downregulating the PPARG signaling pathway-mediated fatty acid oxidation.

(−)-Guaiol inhibits cell proliferation and the invasion ability of lung cancer cells. Cell viability of (−)-guaiol-treated A549 cells was evaluated using the CCK-8 method (Figure 8A). The findings indicated that the concentration of (−)-guaiol required to inhibit cell viability by 50% was 80.73 μM. At concentrations ranging from 10 μM to 40 μM, (−)-guaiol showed no significant cytotoxicity toward A549 cells. (−)-Guaiol markedly inhibited PPARG expression and its downstream targets (CPT1A, CPT1B, CD36) at the proteomic level in A549 cells (Figure 8B). At 10 μM and 30 μM concentrations, (−)-guaiol substantially suppressed A549 cell proliferation, migration, and invasion (Figures 8C–8E).

To verify the generality of (−)-guaiol's effects, we performed additional experiments in H1299 cells (another NSCLC cell line). The CCK-8 assay showed that (−)-guaiol inhibited H1299 cell viability (Figure 8A). Western blot analysis further confirmed that (−)-guaiol downregulated the expression of PPARG and its downstream targets (CPT1A, CPT1B, CD36) in H1299 cells, consistent with the results in A549 cells (Figure 8B). These data indicate that (−)-guaiol's inhibitory effect on NSCLC cells via the PPARG pathway is not cell line-specific.

(−)-Guaiol inhibits the growth of transplanted tumors in lung cancer subcutaneous xenograft mice. Following the conclusion of the experiment, the mice underwent euthanasia, and subcutaneous tumor tissues were dissected and photographed (Figure 9A). Mean body weights were 22.76±0.55 g (control) and 22.58±0.33 g (experimental), showing no significant intergroup difference ($p>0.05$, Figure 9B). (−)-Guaiol significantly inhibited tumor volume and weight (1720.01±246.94 mm^3 vs. 688.828±146.60 mm^3 (Figure 9C); 1.35±0.08 g vs. 0.97±0.03 g (Figure 9D)). Furthermore, (−)-guaiol markedly suppressed the protein expression of PPARG, CPT1A, CPT1B, and CD36 in the subcutaneous xenograft tumor tissues (Figure 9E).

Discussion

Through network pharmacological screening, we identified 91 potential common targets. The top 21 in degree value were ESR1, EGFR, PPARG, PTGS2, HSP90AA1, SRC, GSK3B, PPARA, HMGCR, MAPK14, CYP19A1, KDR, AR, PTPN1, REN, GSTP1, TERT, FABP1, CHEK1, CYP2C19, and CHRM2. There is a high probability that these targets are key targets for the therapeutic potential of (−)-guaiol in lung carcinoma treatment.

PPI analysis revealed that the primary targets of (−)-guaiol in the therapy of pulmonary carcinoma include ESR1, EGFR, PPARG, PTGS2, HSP90AA1, SRC, and HMGCR. Among these, ESR1 was identified as the key target with the highest degree of connectivity. Previous research revealed significantly higher ESR1 methylation levels in peripheral blood from NSCLC patients compared to controls, indicating its possible application as an early detection marker for lung cancer [16]. Research indicates that ESR1 genetic variants may regulate bisphenol A elimination through urine, subsequently affecting lung cancer cell motility and tumor advancement [17]. EGFR expression demonstrates a significant association with lung cancer progression and unfavorable prognosis, serving as a critical driver in NSCLC. In particular, activation of mutant EGFR and its inhibition by specific tyrosine kinase inhibitors (TKIs) can elicit significant tumor responses [18, 19]. EGFR supports the survival and physiological roles of cancer stem cells (CSCs), encompassing stem-like properties maintenance, metabolic regulation, immune-regulatory functions, quiescence, and chemoresistance [20]. Numerous studies demonstrated that PPARG activation can potently suppress NSCLC proliferation and induce apoptosis [21–23]; however, some have also reported that PPARG expression may promote lung cancer growth and invasion. PPARG has been shown to alleviate the inhibitory effect of transforming growth factor-beta (TGFβ) on mitosis in H460 cells [24]. Additionally, PPARG can promote tumor angiogenesis and alter the tumor microenvironment, thereby facilitating the generation of regulatory T cells (Tregs) [9, 25]. Overexpression of PTGS2 induces abundant secretion of exosomal miR-1290, which promotes the activation of cancer-associated fibroblasts and tumor growth in lung adenocarcinoma via the CUL3-Nrf2 pathway [26]. A recent study discovered that β5-integrin can activate tumor cell pyroptosis through the SRC signaling pathway, thereby reversing radiation resistance in lung cancer patients [27]. Furthermore, AMPK may enhance anti-tumor immune responses by suppressing PD-1 in regulatory T cells [28].

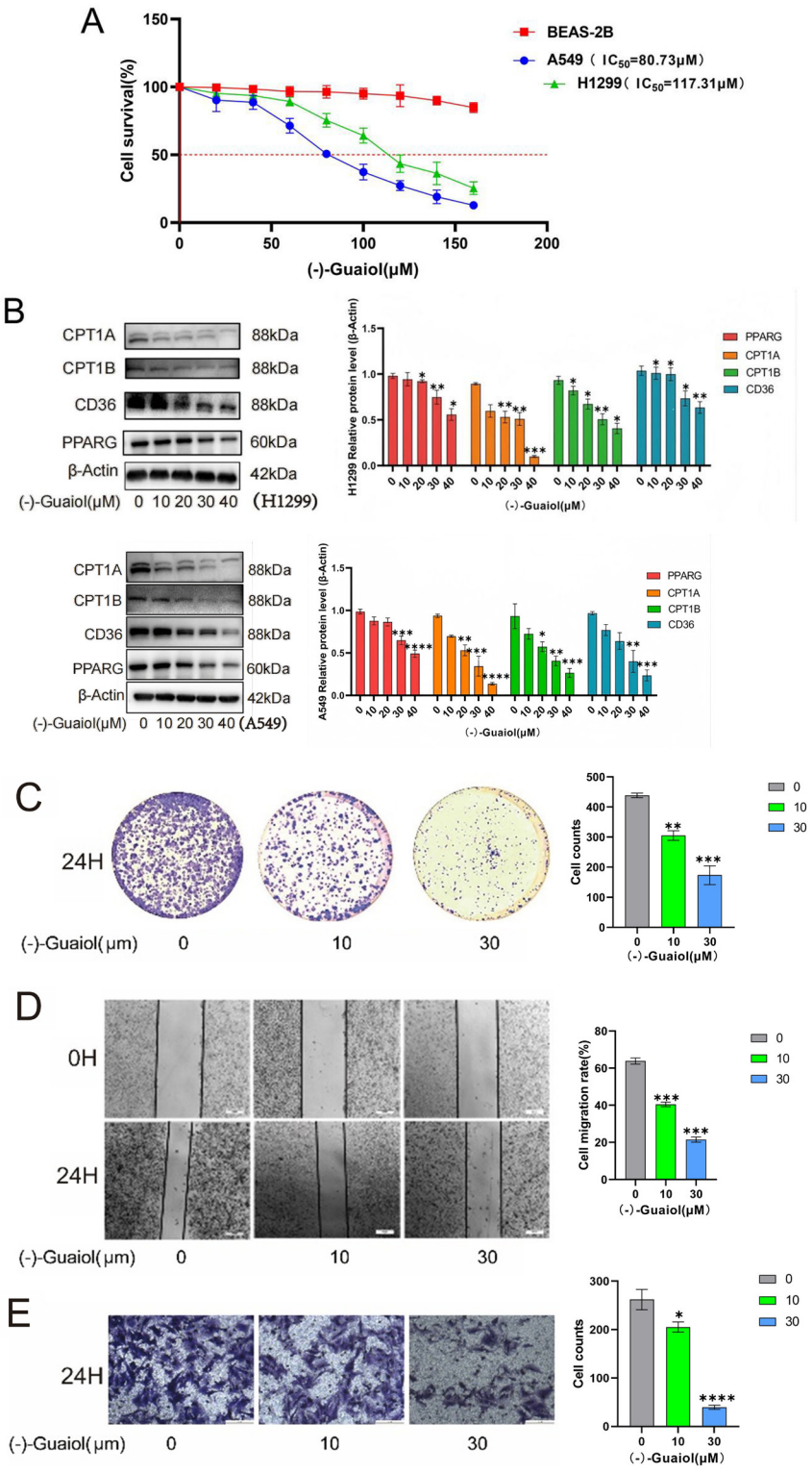

Figure 8. (–)-Guaiol inhibits cell proliferation and invasion ability of lung cancer cells. A) IC50 value of (–)-guaiol on A549 cells and H1299 cells. B) Western Blot to detect the effect of (–)-guaiol on PPARG and its downstream related proteins in A549 cells and H1299 cells. C) Plate cloning experiment to verify the effect of (–)-guaiol on A549 cells' capacity for proliferation. D) Wound healing experiments to verify the effect of (–)-guaiol on migration ability in A549 cells. E) Transwell assay to verify the effect of (–)-guaiol on invasion ability in A549 cells. The control group received 0.1% DMSO (vehicle). All treatments were normalized to equivalent solvent concentration.

GO and KEGG analyses revealed multiple potential mechanisms and the mechanisms by which (–)-guaiol potentially influences its outcomes in lung cancer treatment. GO analysis suggested that (–)-guaiol may influence lung cancer progression via various biological processes, including inflammatory response, apoptosis, CKAP4 signaling pathway, and gastrin signaling pathway. KEGG analysis revealed additional signaling pathways, notably VEGF, PI3K-Akt, and

IL-17 cascades. Previous research indicates (−)-guaiol can inhibit lung adenocarcinoma cell proliferation and induce apoptosis through PI3K/Akt signaling [29]. The VEGF family, which comprises six major isoforms (VEGF121, VEGF145, VEGF165, VEGF183, VEGF189, and VEGF206), is involved in tumor angiogenesis. However, certain VEGF-A isoforms may be expressed through an inhibitory signaling pathway, leading to the arrest of endothelial cell migration and proliferation, thereby exerting an anti-angiogenic effect [30]. The precise mechanism underlying this process remains unclear. The role of the IL-7 signaling pathway in lung cancer has been extensively studied. Current research indicates that IL-7 downregulates autophagy in NSCLC through the P53-mediated AMPK/mTOR cascade [31]. Additionally, IL-7 signaling through the IL-7R-JAK3/STAT5 axis has been shown to enhance chemoresponsiveness in NSCLC cells [32].

Molecular docking studies revealed that (−)-guaiol exhibits varying binding affinities to the screened key targets, with the highest affinity observed for GSK3B. Thus, GSK3B, the mRNA form of GSK-3β, may be a key target of (−)-guaiol in the treatment of lung cancer. One study found that circular RNA circ-GSK3B enhances GSK3β expression by competitively adsorbing miR-3909 and miR-3681-3p, thereby inhibiting the proliferation and motility of lung carcinoma cells

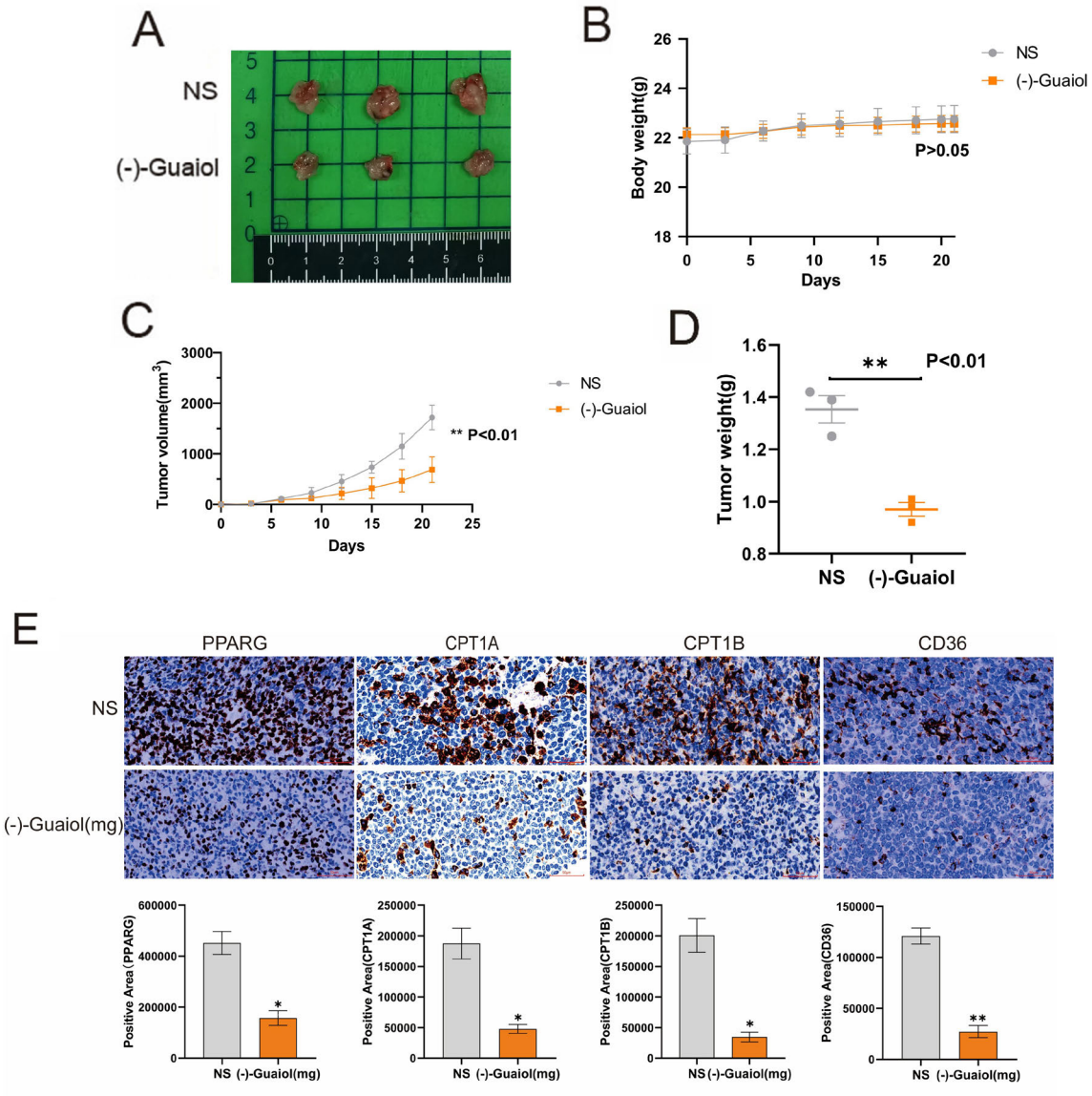

Figure 9. (−)-Guaiol inhibits the growth of transplanted tumors in lung cancer subcutaneous xenograft mice. A) Subcutaneous tumor peeling photographed. B) Mouse body weight change curve. C) Transplanted tumor volume change curve. D) Mouse tumor mass scatter plot. E) Immunohistochemical results of subcutaneous graft tumors in mice after treatment with (−)-guaiol action.

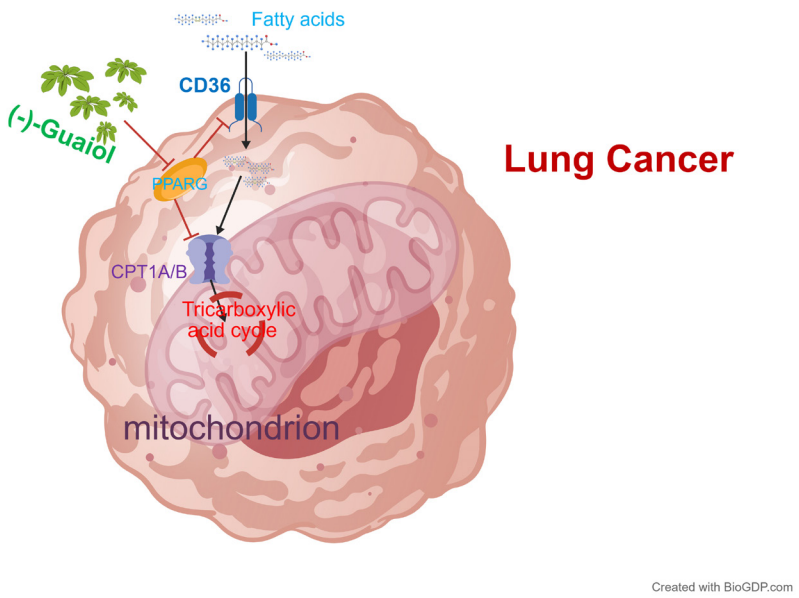

Figure 10. Sketch of the mechanism by which (–)-guaiol modulates the PPARG signaling pathway to inhibit lung cancer.

[33]. Multiple studies have also reported that various other drugs or factors can influence lung cancer cells via GSK-3β. Diosgenin inhibits the proliferation, invasion, and EMT in lung adenocarcinoma mediated by the AKT/GSK3β/mTOR pathway cascade [34]. Astragaloside IV inhibits NSCLC progression through suppression of the AKT/GSK-3β/β-catenin pathway [35]. The lncRNA LINC00222 regulates GSK3β function and enhances apoptosis in NSCLC cells [36]. Deguelin inhibits NSCLC advancement by disrupting EGFR transduction and enhancing GSK3β/FBW7-dependent Mcl-1 proteolysis [37]. Additionally, the interaction between PCNA and GSK3β regulates the apoptosis process in H1299 lung cancer cells [38]. Through mRNA sequencing, we observed that (–)-guaiol downregulates the gene expression of PPARG and CD36, which is consistent with the network pharmacology analysis identifying PPARG as a key target of (–)-guaiol in lung cancer treatment. Notably, PPARG is not an isolated target but is functionally linked to the PI3K/Akt/mTOR signaling axis. Evidence indicates that PPARG enables the PI3K/Akt/mTOR (PAM) pathway by facilitating fatty acid synthase (FASN) activity, leading to significant upregulation of p-mTOR (Ser2481 and Ser2448), PI3K (p85), p-AKT, and p-4EBP1 upon PPARG overexpression [39]. Conversely, PPARG knockdown downregulates these key signaling molecules [39]. Importantly, mTOR inhibition (e.g., with everolimus) has been shown to significantly weaken or abolish the proliferative advantage conferred by PPARG overexpression, demonstrating that PAM pathway activation is central to PPARG-mediated resistance [39]. Given that (–)-guaiol has previously been reported to regulate autophagic cell death via mTOR signaling in NSCLC [14], our current findings suggest that PPARG downregulation may represent an upstream mechanism contributing to mTOR inhibition. Thus, (–)-guaiol may exert its anti-tumor effects through a coordinated suppression of metabolic (PPARG-mediated fatty acid oxidation) and proliferative (PI3K/Akt/mTOR) pathways, extending its previously reported actions on RAD51 and mTOR. Further investigations demonstrated that (–)-guaiol downregulates the PPARG signaling pathway and inhibits the activity of triglyceride lipase. Therefore, we postulate that (–)-guaiol's antitumor activity may involve PPARG regulation, subsequently influencing fatty acid oxidation-associated genes, including CPT1A, CD36, and CPT1B.

To verify these observations and hypotheses, we performed corresponding *in vitro* and *in vivo* studies. Notably, the anti-tumor effects of (–)-guaiol were validated in two NSCLC cell lines (A549 and H1299), with consistent downregulation of the PPARG-mediated fatty acid oxidation pathway and inhibition of cell viability. This consistency across different NSCLC cell lines strengthens the generality of our findings, supporting that (–)-guaiol's mechanism is not restricted to a single cell type. *In vitro* analyses revealed (–)-guaiol's suppression of PPARG expression and modulation of downstream effectors (CPT1A, CPT1B, CD36) in lung cancer cells. Results from Transwell, wound-healing, and colony-formation assays demonstrated that (–)-guaiol significantly inhibited the invasive capacity, migration, and proliferation of lung cancer cells. Meanwhile, *in vivo* animal experiments also revealed that (–)-guaiol inhibited the growth of transplanted Lewis lung carcinoma tumors in mice. Furthermore, immunohistochemical results showed that (–)-guaiol significantly suppressed the expression of PPARG and its downstream pathway components – CPT1A, CPT1B,

and CD36 – in lung cancer tissues. After clarifying the correlation between (–)-guaiol and the fatty acid oxidation process in lung cancer, as well as its molecular mechanism of action, we illustrated a schematic diagram of (–)-guaiol-mediated regulation of fatty acid oxidation in lung cancer in Figure 10 (created with BioGDP.com [40]).

However, this study still has the following limitations. First, the differential roles of PPARG in tumor cells and stromal cells require further validation through more precise cell-specific knock-out experiments. Second, the relationship between fatty acid oxidation inhibition and the function of immune effector cells warrants further investigation. Finally, the pharmacokinetic characteristics of (–)-guaiol require validation in larger cohorts.

In conclusion, through integrated network pharmacology, molecular dynamics, transcriptomic analysis, and experimental validation, this study reveals (–)-guaiol's potent suppression of lung cancer cell invasion, migration, and proliferation via PPARG-mediated fatty acid metabolism. The compound exhibits polypharmacological activity targeting multiple pathways, including ESR1/GSK3B/PPARG signaling, lipid metabolism, inflammation, apoptosis, and IL-17/VEGF/PI3K-Akt axes.

Supplementary information is available in the online version of the paper.

Acknowledgments: This work was supported by the Shanghai University of Traditional Chinese Medicine Science and Technology Development Project (24KFL090); The National Natural Science Foundation of China (No.82204842, No.82174183, No.82575159); The YangFan project from the Science and Technology Commission of Shanghai Municipality (No. 22YF1445400); Shanghai Three-year Action Plan to Further Accelerate the Development of Traditional Chinese Medicine Inheritance and Innovation (2021–2023) (No. ZY(2021-2023)-0211), and Shanghai famous old Chinese medicine academic experience research studio construction project (No. SHGZS-202210).

References

[1] BRODY H. Lung cancer. Nature 2020; 587: S7. https://doi.org/10.1038/d41586-020-03152-0

[2] WEI X, PNG CW, WEERASOORIYA M, LI H, ZHU C et al. Tumor Promoting Function of DUSP10 in Non-Small Cell Lung Cancer Is Associated With Tumor-Promoting Cytokines. Immune Netw 2023; 23: e34. https://doi.org/10.4110/in.2023.23.e34

[3] MAHARATI A, MOGHBELI M. Role of microRNAs in regulation of doxorubicin and paclitaxel responses in lung tumor cells. Cell Div 2023; 18: 11. https://doi.org/10.1186/s13008-023-00093-8

[4] WANG F, YANG M, LUO W, ZHOU Q. Characteristics of tumor microenvironment and novel immunotherapeutic strategies for non-small cell lung cancer. J Natl Cancer Cent 2022; 2: 243–262. https://doi.org/10.1016/j.jncc.2022.10.002

[5] HU T, HAN F, AN Z. Comprehensive profiling of serum glycosphingolipids to discover the diagnostic biomarkers of lung cancer and uncover the variation of glycosphingolipid networks in different lung cancer subtypes. Anal Methods 2024; 16: 7873–7887. https://doi.org/10.1039/d4ay01685h

[6] ZHANG J, TANG M, SHANG J. PPARγ Modulators in Lung Cancer: Molecular Mechanisms, Clinical Prospects, and Challenges. Biomolecules 2024; 14: 190. https://doi.org/10.3390/biom14020190

[7] MANGRAL ZA, BHAT BA, SHEIKH S, ISLAM SU, TARIQ L et al. Exploring the therapeutic potential of Rhododendron anthopogon D.Don essential oil constituents against lung cancer: A network pharmacology-based analysis with molecular docking and experimental studies. Comput Biol Med 2025; 187: 109827. https://doi.org/10.1016/j.compbiomed.2025.109827

[8] YANG PB, HOU PP, LIU FY, HONG WB, CHEN HZ et al. Blocking PPARγ interaction facilitates Nur77 interdiction of fatty acid uptake and suppresses breast cancer progression. Proc Natl Acad Sci U S A 2020; 117: 27412–27422. https://doi.org/10.1073/pnas.2002997117

[9] ZHANG H, ZHU K, ZHANG R, GUO Y, WANG J et al. Oleic acid-PPARγ-FABP4 loop fuels cholangiocarcinoma colonization in lymph node metastases microenvironment. Hepatology 2024, 80: 69–86. https://doi.org/10.1097/HEP.0000000000000784

[10] TANG W, SUN G, JI GW, FENG T, ZHANG Q et al. Single-cell RNA-sequencing atlas reveals an FABP1-dependent immunosuppressive environment in hepatocellular carcinoma. J Immunother Cancer 2023; 11: e007030. https://doi.org/10.1136/jitc-2023-007030

[11] CHOUDHARY MI, BATOOL I, ATIF M, HUSSAIN S, ATTA UR R. Microbial transformation of (–)-guaiol and antibacterial activity of its transformed products. J Nat Prod 2007; 70: 849–852. https://doi.org/10.1021/np068052a

[12] YANG X, YANG J, GU X, TAO Y, JI H et al. (–)-Guaiol triggers immunogenic cell death and inhibits tumor growth in non-small cell lung cancer. Mol Cell Biochem 2023; 478: 1611–1620. https://doi.org/10.1007/s11010-022-04613-y

[13] CAO Y, WU Y, TU H, GU Z, YU F et al. (–)-Guaiol inhibit epithelial-mesenchymal transition in lung cancer via suppressing M2 macrophages mediated STAT3 signaling pathway. Heliyon 2023; 9: e19817. https://doi.org/10.1016/j.heliyon.2023.e19817

[14] YANG X, ZHU J, WU J, HUANG N, CUI Z et al. (–)-Guaiol regulates autophagic cell death depending on mTOR signaling in NSCLC. Cancer Biol Ther 2018; 19: 706–714. https://doi.org/10.1080/15384047.2018.1451277

[15] TAN B, LAN X, ZHANG Y, LIU P, JIN Q et al. Effect of 23-hydroxybetulinic acid on lung adenocarcinoma and its mechanism of action. Exp Ther Med 2024; 27: 239. https://doi.org/10.3892/etm.2024.12527

[16] FAN XP, DOU CY, FAN YC, CAO CJ, ZHAO ZH et al. Methylation status of the estrogen receptor 1 promoter predicts poor prognosis of acute-on-chronic hepatitis B liver failure. Rev Esp Enferm Dig 2017; 109: 818–827. https://doi.org/10.17235/reed.2017.4426/2016

[17] LI J, JI Z, LUO X, LI Y, YUAN P et al. Urinary bisphenol A and its interaction with ESR1 genetic polymorphism associated with non-small cell lung cancer: findings from a case-control study in Chinese population. Chemosphere 2020, 254: 126835. https://doi.org/10.1016/j.chemosphere.2020.126835
[18] CHENG FJ, CHEN CH, TSAI WC, WANG BW, YU MC et al. Cigarette smoke-induced LKB1/AMPK pathway deficiency reduces EGFR TKI sensitivity in NSCLC. Oncogene 2021; 40: 1162–1175. https://doi.org/10.1038/s41388-020-01597-1
[19] TESSEMA M, ROSSI MR, PICCHI MA, YINGLING CM, LIN Y et al. Common cancer-driver mutations and their association with abnormally methylated genes in lung adenocarcinoma from never-smokers. Lung Cancer 2018; 123: 99–106. https://doi.org/10.1016/j.lungcan.2018.07.011
[20] XU Z, QIN F, YUAN L, WEI J, SUN Y et al. EGFR DNA Methylation Correlates With EGFR Expression, Immune Cell Infiltration, and Overall Survival in Lung Adenocarcinoma. Front Oncol 2021; 11: 691915. https://doi.org/10.3389/fonc.2021.691915
[21] TU H, FENG Y, WANG W, ZHOU H, CAI Q et al. Exploring the mechanism of bioactive components of Prunella vulgaris L. in treating hepatocellular carcinoma based on network pharmacology. Chem Biol Drug Des 2024; 103: e14413. https://doi.org/10.1111/cbdd.14413
[22] ZHOU S, WANG Y, XIE M, LI J, MENG P et al. Uncovering the antidepressant active ingredients and related molecular mechanisms of Xiaoyao Pill using integrated pharmacological strategy. J Chromatogr B Analyt Technol Biomed Life Sci 2025; 1255: 124502. https://doi.org/10.1016/j.jchromb.2025.124502
[23] WEI M, LI H, LI Q, QIAO Y, MA Q et al. Based on Network Pharmacology to Explore the Molecular Targets and Mechanisms of Gegen Qinlian Decoction for the Treatment of Ulcerative Colitis. Biomed Res Int 2020; 2020: 5217405. https://doi.org/10.1155/2020/5217405
[24] LI JD, FENG QC, QI Y, CUI G, ZHAO S. PPARGC1A is upregulated and facilitates lung cancer metastasis. Exp Cell Res 2017; 359: 356–360. https://doi.org/10.1016/j.yexcr.2017.08.017
[25] LIU R, WANG J, ZHANG L, WANG S, LI X et al. GLIDR-mediated regulation of tumor malignancy and cisplatin resistance in non-small cell lung cancer via the miR-342-5p/PPARGC1A axis. BMC Cancer 2024; 24: 1126. https://doi.org/10.1186/s12885-024-12845-y
[26] BAI X, SHAO J, DUAN T, LIU X, WANG M et al. Exo-miR-1290-induced by COX-2 overexpression promotes cancer-associated fibroblasts activation and tumor progression by CUL3-Nrf2 pathway in lung adenocarcinoma. Cell Commun Signal 2023; 21: 242. https://doi.org/10.1186/s12964-023-01268-0
[27] SU L, CHEN Y, HUANG C, WU S, WANG X et al. Targeting Src reactivates pyroptosis to reverse chemoresistance in lung and pancreatic cancer models. Sci Transl Med 2023; 15: eabl7895. https://doi.org/10.1126/scitranslmed.abl7895
[28] POKHREL RH, ACHARYA S, AHN JH, GU Y, PANDIT M et al. AMPK promotes antitumor immunity by downregulating PD-1 in regulatory T cells via the HMGCR/p38 signaling pathway. Mol Cancer 2021; 20: 133. https://doi.org/10.1186/s12943-021-01420-9
[29] ZENG Y, PAN Y, ZHANG B, LUO Y, TIAN J et al. Integrating Network Pharmacology, Molecular Docking, and Experimental Validation to Investigate the Mechanism of (–)-Guaiol Against Lung Adenocarcinoma. Med Sci Monit 2022; 28: e937131. https://doi.org/10.12659/MSM.937131
[30] ZHANG T, QIAN Y, YUAN C, WU Y, QIAN H et al. Propranolol Suppresses Proliferation and Migration of HUVECs through Regulation of the miR-206/VEGFA Axis. Biomed Res Int 2021; 2021: 7629176. https://doi.org/10.1155/2021/7629176
[31] ZHU Y, JIANG X, DING Z, MING J. Interleukin 7 inhibit autophagy via P53 regulated AMPK/mTOR signaling pathway in non-small cell lung cancer. Sci Rep 2022; 12: 11208. https://doi.org/10.1038/s41598-022-14742-5
[32] SHI L, XU Z, YANG Q, HUANG Y, GONG Y et al. IL-7-Mediated IL-7R-JAK3/STAT5 signalling pathway contributes to chemotherapeutic sensitivity in non-small-cell lung cancer. Cell Prolif 2019; 52: e12699. https://doi.org/10.1111/cpr.12699
[33] ZHU MC, ZHANG YH, XIONG P, FAN XW, LI GL et al. Circ-GSK3B up-regulates GSK3B to suppress the progression of lung adenocarcinoma. Cancer Gene Ther 2022; 29: 1761–1772. https://doi.org/10.1038/s41417-022-00489-8
[34] MAO W, YIN H, CHEN W, ZHAO T, WU S et al. Network Pharmacology and Experimental Evidence Reveal Dioscin Suppresses Proliferation, Invasion, and EMT via AKT/GSK3b/mTOR Signaling in Lung Adenocarcinoma. Drug Des Devel Ther 2020; 14: 2135–2147. https://doi.org/10.2147/DDDT.S249651
[35] JIA L, LV D, ZHANG S, WANG Z, ZHOU B. Astragaloside IV Inhibits the Progression of Non-Small Cell Lung Cancer Through the Akt/GSK-3β/β-Catenin Pathway. Oncol Res 2019; 27: 503–508. https://doi.org/10.3727/096504018X15344989701565
[36] ZHANG H, WANG Y, LU J, ZHAO Y. Long non-coding RNA LINC00222 regulates GSK3β activity and promotes cell apoptosis in lung adenocarcinoma. Biomed Pharmacother 2018; 106: 755–762. https://doi.org/10.1016/j.biopha.2018.06.165
[37] Gao F, Yu X, Li M, Zhou L, Liu W et al. Deguelin suppresses non-small cell lung cancer by inhibiting EGFR signaling and promoting GSK3β/FBW7-mediated Mcl-1 destabilization. Cell Death Dis 2020; 11: 143. https://doi.org/10.1038/s41419-020-2344-0
[38] LIU XH, TANG DE, DAI Y, GAO XJ, LIU LX. PCNA and GSK3β interact with each other to regulate H1299 lung adenocarcinoma cells apoptosis. Neoplasma 2020; 67: 15–26. https://doi.org/10.4149/neo_2019_190116N48
[39] XIONG M, LIU D, WANG X, REN H, CHI W et al. PPARG Activation of Fatty Acid Metabolism Drives Resistance to Anti-HER2 Therapies in HER2-Positive Breast Cancer. Int J Biol Sci 2025; 21: 2396–2414. https://doi.org/10.7150/ijbs.99275
[40] JIANG S, LI H, ZHANG L, MU W, ZHANG Y et al. Generic Diagramming Platform (GDP): a comprehensive database of high-quality biomedical graphics. Nucleic Acids Res 2025; 53: D1670–D1676. https://doi.org/10.1093/nar/gkae973

https://doi.org/10.4149/neo_2026_251111N475

(–)-Guaiol inhibits lung cancer via PPARG-dependent fatty acid oxidation

Zhen-Yu ZHAO[1,#], Bo ZHANG[1,#], Ying-Bin LUO[1], Xing-Yu WANG[2], Yu-Li WANG[1], Xi WANG[1], Jian-Hui TIAN[1], Jian-Chun WU[1,*], Yan LI[1]

Supplementary Information

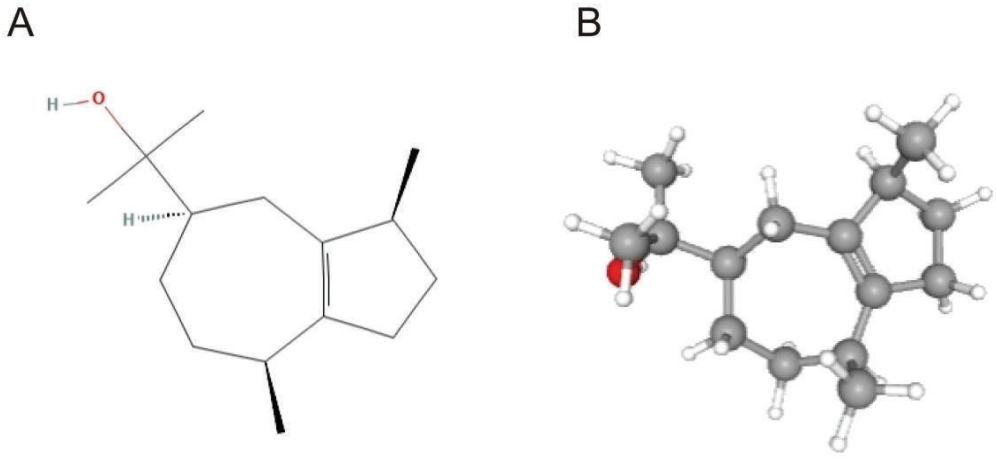

Supplementary Figure S1. A 2D Structure of (–)-Guaiol; B 3D structure of (–)-Guaiol.

Supplementary Table S1. Gene names of key targets, Degree values, Closeness centrality and Betweenness centrality.

Gene name	Degree value	Closeness centrality	Betweenness centrality
ESR1	33	0.57419355	0.1113184
EGFR	32	0.55974843	0.12843102
PPARG	31	0.55625	0.07630315
PTGS2	29	0.58169935	0.14750825
HSP90AA1	29	0.54601227	0.10285462
SRC	25	0.54938272	0.0913787
GSK3B	24	0.4972067	0.04546845
PPARA	23	0.51744186	0.03588086
HMGCR	22	0.52662722	0.04191891
MAPK14	20	0.50568182	0.03028077
CYP19A1	19	0.50857143	0.03648895
KDR	18	0.50282486	0.02297985
AR	17	0.50857143	0.01798621
PTPN1	15	0.47089947	0.02350635
REN	14	0.47089947	0.03402625
GSTP1	13	0.47089947	0.02314732
TERT	13	0.47340426	0.02168369
FABP1	13	0.45177665	0.02335122
CHEK1	11	0.43414634	0.0246155
CYP2C19	11	0.44278607	0.0326167
CHRM2	10	0.41203704	0.03446309

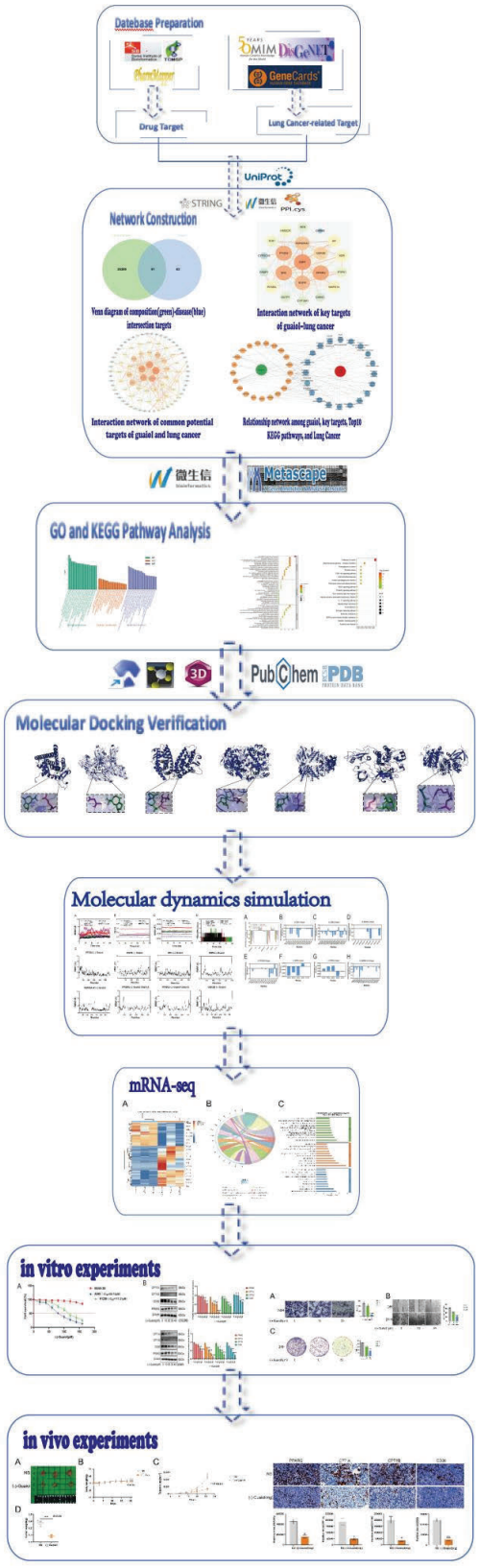

Supplementary Figure S2. Flowchart for Exploring the Molecular Mechanism of Action of (–)-Guaiol for the Treatment of Lung Cancer, Using Network Pharmacology, mRNA Sequencing and Experimental Validation.

Supplementary Table S2. KEGG pathway annotation with TOP20 enrichment level and the possible targets involved.

KEGG pathways	Enrichment degree	Target count	Targets
Pathways in cancer	0.428571429	9	AR|EGFR|ESR1|GSK3B|GSTP1|HSP90AA1|PPARG|PTGS2|TERT
Chemical carcinogenesis-receptor activation	0.285714286	6	AR|EGFR|ESR1|HSP90AA1|PPARA|SRC
Prostate cancer	0.238095238	5	AR|EGFR|GSK3B|GSTP1|HSP90AA1
Fluid shear stress and atherosclerosis	0.238095238	5	MAPK14|GSTP1|HSP90AA1|KDR|SRC
Proteoglycans in cancer	0.238095238	4	MAPK14|KDR|PTGS2|SRC
Lipid and atherosclerosis	0.238095238	4	MAPK14|ESR1|GSK3B|SRC
Human cytomegalovirus infection	0.238095238	4	GSK3B|SRC|KDR|EGFR
PI3K-Akt signaling pathway	0.238095238	5	MAPK14|EGFR|ESR1|KDR|SRC
VEGF signaling pathway	0.19047619	5	MAPK14|GSK3B|HSP90AA1|PPARG|SRC
Prolactin signaling pathway	0.19047619	5	MAPK14|EGFR|GSK3B|PTGS2|SRC
EGFR tyrosine kinase inhibitor resistance	0.19047619	4	MAPK14|GSK3B|HSP90AA1|PTGS2
Endocrine resistance	0.19047619	4	MAPK14|EGFR|ESR1|SRC
Estrogen signaling pathway	0.19047619	4	EGFR|ESR1|HSP90AA1|SRC
Alcoholic liver disease	0.19047619	4	MAPK14|FABP1|GSK3B|PPARA
Non-alcoholic fatty liver disease	0.19047619	4	MAPK14|GSK3B|PPARA|PPARG
Hepatocellular carcinoma	0.19047619	5	CHRM2|EGFR|GSK3B|HSP90AA1|KDR
Kaposi sarcoma-associated herpesvirus infection	0.19047619	4	EGFR|GSK3B|GSTP1|TERT
Focal adhesion	0.19047619	4	MAPK14|GSK3B|PTGS2|SRC
Diabetic cardiomyopathy	0.19047619	4	EGFR|GSK3B|KDR|SRC
IL-17 signaling pathway	0.19047619	4	MAPK14|GSK3B|PPARA|REN

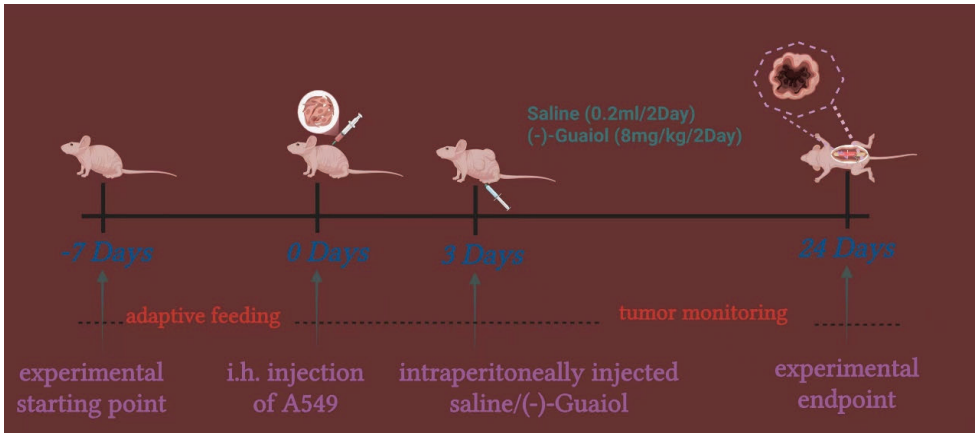

Supplementary Figure S3. Flow chart of animal modeling.

Supplementary Table S3. Binding energies of (−)-Guaiol to various key targets.

Key target	PDBID	Binding energy (kcal/mol)
ESR1	3ERT	-7.52
EGFR	5WB7	-5.27
PPARG	6T9C	-7.01
PTGS2	5FDQ	-7.38
HSP90AA1	7KRJ	-5.73
SRC	2H8H	-7.61
GSK3B	4ACH	-7.71

https://doi.org/10.4149/neo_2026_251111N475

(–)-Guaiol inhibits lung cancer via PPARG-dependent fatty acid oxidation

Zhen-Yu ZHAO[1,#], Bo ZHANG[1,#], Ying-Bin LUO[1], Xing-Yu WANG[2], Yu-Li WANG[1], Xi WANG[1], Jian-Hui TIAN[1], Jian-Chun WU[1,*], Yan LI[1]

Supplementary Information

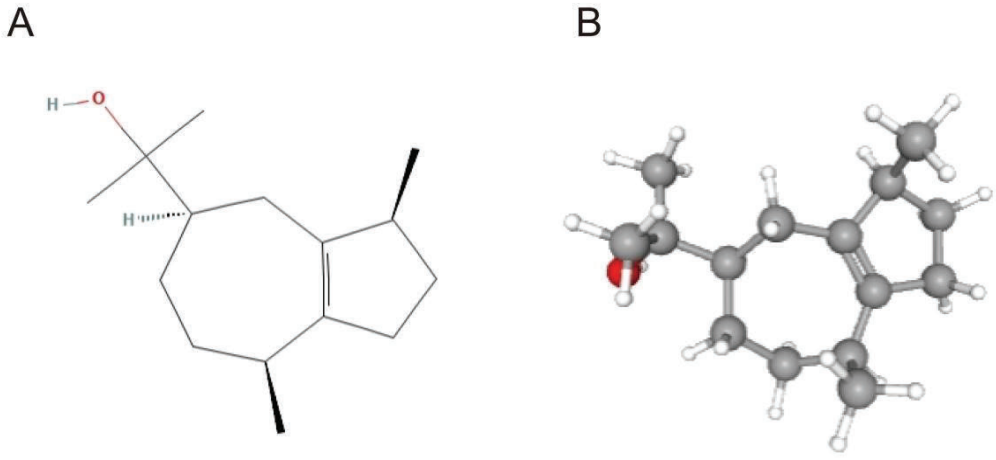

Supplementary Figure S1. A 2D Structure of (–)-Guaiol; B 3D structure of (–)-Guaiol.

Supplementary Table S1. Gene names of key targets, Degree values, Closeness centrality and Betweenness centrality.

Gene name	Degree value	Closeness centrality	Betweenness centrality
ESR1	33	0.57419355	0.1113184
EGFR	32	0.55974843	0.12843102
PPARG	31	0.55625	0.07630315
PTGS2	29	0.58169935	0.14750825
HSP90AA1	29	0.54601227	0.10285462
SRC	25	0.54938272	0.0913787
GSK3B	24	0.4972067	0.04546845
PPARA	23	0.51744186	0.03588086
HMGCR	22	0.52662722	0.04191891
MAPK14	20	0.50568182	0.03028077
CYP19A1	19	0.50857143	0.03648895
KDR	18	0.50282486	0.02297985
AR	17	0.50857143	0.01798621
PTPN1	15	0.47089947	0.02350635
REN	14	0.47089947	0.03402625
GSTP1	13	0.47089947	0.02314732
TERT	13	0.47340426	0.02168369
FABP1	13	0.45177665	0.02335122
CHEK1	11	0.43414634	0.0246155
CYP2C19	11	0.44278607	0.0326167
CHRM2	10	0.41203704	0.03446309

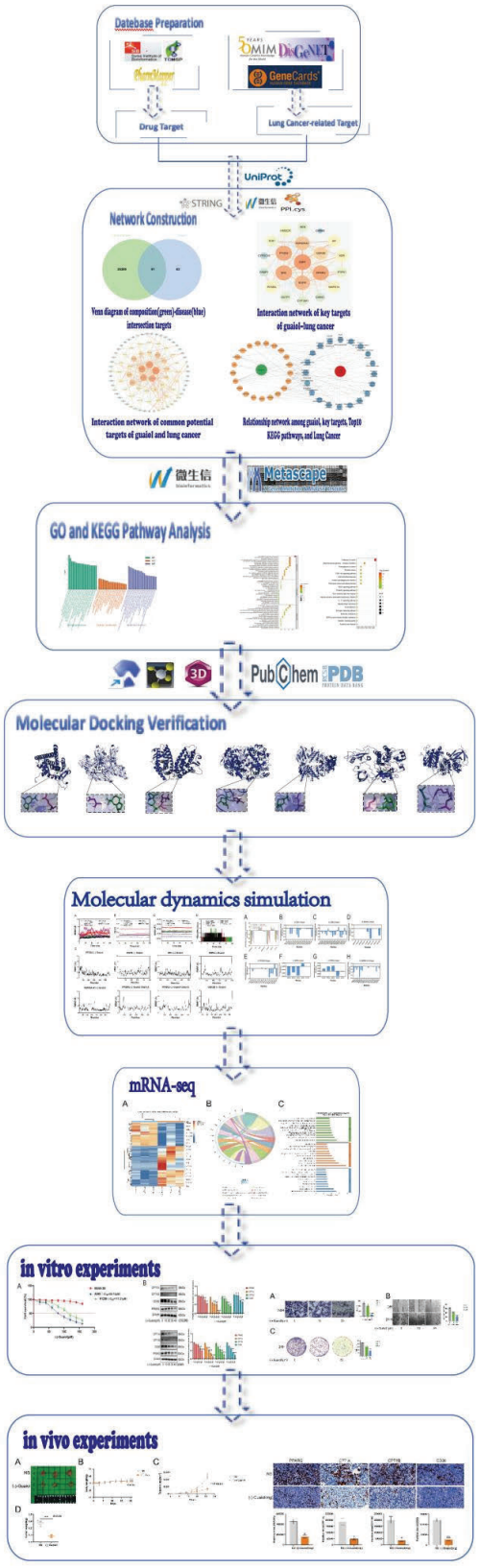

Supplementary Figure S2. Flowchart for Exploring the Molecular Mechanism of Action of (–)-Guaiol for the Treatment of Lung Cancer, Using Network Pharmacology, mRNA Sequencing and Experimental Validation.

Supplementary Table S2. KEGG pathway annotation with TOP20 enrichment level and the possible targets involved.

KEGG pathways	Enrichment degree	Target count	Targets
Pathways in cancer	0.428571429	9	AR|EGFR|ESR1|GSK3B|GSTP1|HSP90AA1|PPARG|PTGS2|TERT
Chemical carcinogenesis-receptor activation	0.285714286	6	AR|EGFR|ESR1|HSP90AA1|PPARA|SRC
Prostate cancer	0.238095238	5	AR|EGFR|GSK3B|GSTP1|HSP90AA1
Fluid shear stress and atherosclerosis	0.238095238	5	MAPK14|GSTP1|HSP90AA1|KDR|SRC
Proteoglycans in cancer	0.238095238	4	MAPK14|KDR|PTGS2|SRC
Lipid and atherosclerosis	0.238095238	4	MAPK14|ESR1|GSK3B|SRC
Human cytomegalovirus infection	0.238095238	4	GSK3B|SRC|KDR|EGFR
PI3K-Akt signaling pathway	0.238095238	5	MAPK14|EGFR|ESR1|KDR|SRC
VEGF signaling pathway	0.19047619	5	MAPK14|GSK3B|HSP90AA1|PPARG|SRC
Prolactin signaling pathway	0.19047619	5	MAPK14|EGFR|GSK3B|PTGS2|SRC
EGFR tyrosine kinase inhibitor resistance	0.19047619	4	MAPK14|GSK3B|HSP90AA1|PTGS2
Endocrine resistance	0.19047619	4	MAPK14|EGFR|ESR1|SRC
Estrogen signaling pathway	0.19047619	4	EGFR|ESR1|HSP90AA1|SRC
Alcoholic liver disease	0.19047619	4	MAPK14|FABP1|GSK3B|PPARA
Non-alcoholic fatty liver disease	0.19047619	4	MAPK14|GSK3B|PPARA|PPARG
Hepatocellular carcinoma	0.19047619	5	CHRM2|EGFR|GSK3B|HSP90AA1|KDR
Kaposi sarcoma-associated herpesvirus infection	0.19047619	4	EGFR|GSK3B|GSTP1|TERT
Focal adhesion	0.19047619	4	MAPK14|GSK3B|PTGS2|SRC
Diabetic cardiomyopathy	0.19047619	4	EGFR|GSK3B|KDR|SRC
IL-17 signaling pathway	0.19047619	4	MAPK14|GSK3B|PPARA|REN

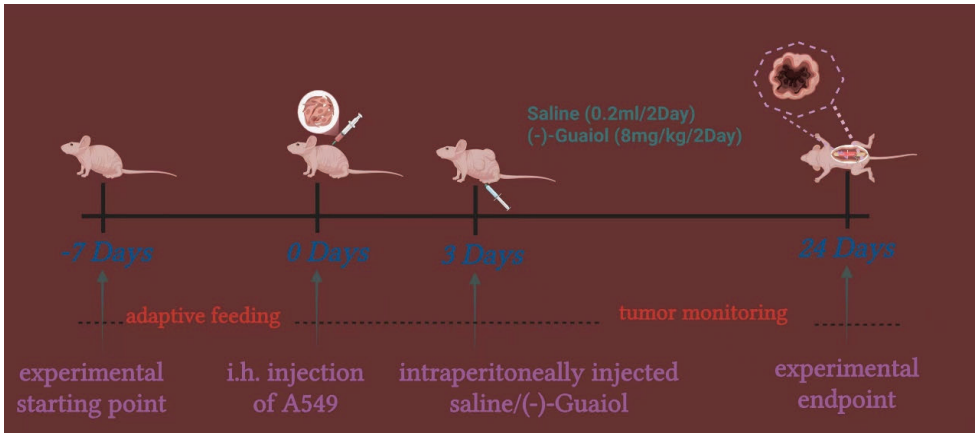

Supplementary Figure S3. Flow chart of animal modeling.

Supplementary Table S3. Binding energies of (−)-Guaiol to various key targets.

Key target	PDBID	Binding energy (kcal/mol)
ESR1	3ERT	-7.52
EGFR	5WB7	-5.27
PPARG	6T9C	-7.01
PTGS2	5FDQ	-7.38
HSP90AA1	7KRJ	-5.73
SRC	2H8H	-7.61
GSK3B	4ACH	-7.71